Atmospheric
Chemistry
and Physics

NH$_3$ spatiotemporal variability over Paris, Mexico City, and Toronto, and its link to PM$_{2.5}$ during pollution events

Camille Viatte[1], **Rimal Abeed**[1], **Shoma Yamanouchi**[2,3], **William C. Porter**[4], **Sarah Safieddine**[1],
Martin Van Damme[5,6], **Lieven Clarisse**[4], **Beatriz Herrera**[2,7], **Michel Grutter**[7], **Pierre-Francois Coheur**[4],
Kimberly Strong[2], and **Cathy Clerbaux**[1,5]

[1]LATMOS/IPSL, Sorbonne Université, UVSQ, CNRS, 75252 Paris CEDEX 05, France
[2]Department of Physics, University of Toronto, Toronto ON M5S 1A7, Canada
[3]Department of Civil and Mineral Engineering, University of Toronto, Toronto ON M5S 1A4, Canada
[4]Department of Environmental Sciences, University of California, Riverside, CA 92521, USA
[5]Spectroscopy, Quantum Chemistry and Atmospheric Remote Sensing (SQUARES),
Université libre de Bruxelles (ULB), Brussels 1050, Belgium
[6]BIRA-IASB – Belgian Institute for Space Aeronomy, Brussels 1180, Belgium
[7]Instituto de Ciencias de la Atmósfera y Cambio Climático, Universidad Nacional Autónoma de México,
Mexico City, 04510, Mexico

Correspondence: Camille Viatte (camille.viatte@latmos.ipsl.fr)

Abstract. Megacities can experience high levels of fine particulate matter (PM$_{2.5}$) pollution linked to ammonia (NH$_3$) mainly emitted from agricultural activities. Here, we investigate such pollution in the cities of Paris, Mexico, and Toronto, each of which have distinct emission sources, agricultural regulations, and topography. Ten years of measurements from the infrared atmospheric sounding interferometer (IASI) are used to assess the spatiotemporal NH$_3$ variability over and around the three cities.

In Europe and North America, we determine that temperature is associated with the increase in NH$_3$ atmospheric concentrations with a coefficient of determination (r^2) of 0.8 over agricultural areas. The variety of the NH$_3$ sources (industry and agricultural) and the weaker temperature seasonal cycle in southern North America induce a lower correlation factor ($r^2 = 0.5$). The three regions are subject to long-range transport of NH$_3$, as shown using HYSPLIT cluster back trajectories. The highest NH$_3$ concentrations measured at the city scale are associated with air masses coming from the surrounding and north/northeast regions of Paris, the south/southwest areas of Toronto, and the southeast/southwest zones of Mexico City.

Using NH$_3$ and PM$_{2.5}$ measurements derived from IASI and surface observations from 2008 to 2017, annually frequent pollution events are identified in the three cities. Wind roses reveal statistical patterns during these pollution events with dominant northeast/southwest directions in Paris and Mexico City, and the transboundary transport of pollutants from the United States in Toronto. To check how well chemistry transport models perform during pollution events, we evaluate simulations made using the GEOS-Chem model for March 2011. In these simulations we find that NH$_3$ concentrations are underestimated overall, though day-to-day variability is well represented. PM$_{2.5}$ is generally underestimated over Paris and Mexico City, but overestimated over Toronto.

1 Introduction

Paris, Toronto, and Mexico City are cities with over 2 million inhabitants. When their larger metropolitan regions are included, their populations are 10.5 million for Paris (the most populous area in the European Union), 6.5 million for Toronto (the fourth most populous city in North America), and 9.2 million for Mexico City (the most populous city in North America). These cities typically experience strong particulate matter (PM) pollution episodes. Exposure to such particles is harmful to humans and can lead to cardiovascular and respiratory diseases (Murray et al., 2020).

A large proportion of the particles' composition is ammonium sulfate and nitrate, which are formed from ammonia (NH$_3$) (Behera et al., 2013) released into the atmosphere from, e.g., fertilizer spreading practices and both transported to cities, reducing the quality of urban air (Pope et al., 2009). The agricultural sector represents 94 %, 90 %, and 94 % of total NH$_3$ emissions in France (CITEPA, 2018), Canada (ECCC, 2022), and Mexico (INECC and SEMARNAT, 2018), respectively. NH$_3$ is the most poorly understood precursor of PM$_{2.5}$ (PM with a diameter less than 2.5 μm), primarily because measurements are difficult (von Bobrutzki et al., 2010), sparse, and due to low ambient NH$_3$ concentrations and episodic emissions. Worldwide, only five countries (United States, China, the Netherlands, United Kingdom, and Canada) have included routine measurements of NH$_3$ concentrations in their air quality monitoring networks (Nair and Yu, 2020).

NH$_3$ emissions are associated with very high uncertainties in all inventories (186 % to 294 % uncertainties in EDGAR; McDuffie et al., 2021; Van Damme et al., 2018) due to uncertainties in the reporting of agricultural statistics and emission factors that depend on individual agricultural practices, biological processes, and environmental conditions (Paulot and Jacob, 2014), as well as political disturbances and land-use change (Abeed et al., 2021). The evaporation of NH$_3$ in the atmosphere, as well as its transformation into particulate matter, is highly dependent on the thermodynamic conditions of the atmosphere (Sutton et al., 2013). All these parameters account for the complexity of reproducing NH$_3$ concentrations in atmospheric models, predicting the associated PM$_{2.5}$ pollution, and, ultimately, implementing relevant regulations to reduce its emissions.

Given the crucial role that NH$_3$ plays in environmental and public health problems, reducing its emissions will be a major challenge. However, NH$_3$ concentrations are increasing in many countries: France, Canada, and Mexico reported increases of 24 ± 11 %, 16.4 ± 8.6 %, and 8.4 ± 5.2 % between 2008 and 2018, respectively (Van Damme et al., 2021). These trends are likely explained by increasing emissions, partly due to increased temperature (Europe) and biomass burning (Canada). However, decreasing concentrations of nitrogen and sulfur oxides, e.g., in Europe and China, also increase

the ammonia atmospheric lifetime and play a role in the reported upward trends.

In Paris, PM$_{2.5}$ are composed of organic matter (38 %–47 %), nitrate (17 %–22 %), non-sea-salt sulfate (13 %–16 %), ammonium (10 %–12 %), and, to a minor extent, elemental carbon, mineral dust (2 %–5 %), and sea salt (Bressi et al., 2014). In spring, it has been shown that NH$_3$ plays a significant role in PM$_{2.5}$ pollution episodes (Viatte et al., 2021), but long-term observations are needed to properly evaluate the impact of NH$_3$ to PM$_{2.5}$ formation.

In Toronto, secondary nitrate formed from nitric acids (NO$_x$) and NH$_3$ account for 36 % of the PM$_{2.5}$ sources (Lee et al., 2003) and ammonium nitrate and sulfate accounted for 20 %–30 % of annual PM$_{2.5}$ mass over the 14-year period between 2004 and 2017 (Jeong et al., 2020). There is a need for a higher number of surface observations to evaluate the NH$_3$–PM$_{2.5}$ relationship and its evolution over time (Larios et al., 2018).

In Mexico, PM$_{2.5}$ concentrations often exceed the national standard of 41 μg m^{-3} for the 24 h mean (NOM-025-SSA1-2021, 2021). Secondary inorganic aerosols, which are dominated by ammonium sulfate with an average of 14 %, account for 30 % of the chemical composition of PM$_{2.5}$ (Vega et al., 2010). A better understanding of the particulate pollutants processes in Mexico is still needed (Ojeda-Castillo et al., 2019).

To assess the role of NH$_3$ in the formation of particulate matter, the AmmonAQ (ammonia air quality) project was designed to quantify NH$_3$ spatiotemporal variabilities in regional domains around these three cities. The main objective of this project is to determine the impact of intensive agricultural practices on NH$_3$ and urban air quality, with a focus on Paris, Toronto, and Mexico as benchmark case studies. A schematic representation of the AmmonAQ project and the domains of study are shown in Fig. 1. The "Europe", "North America", and "southern North America" domains represent the extended area with NH$_3$ sources that can impact the Paris, Toronto, and Mexico City air composition. The three cities are investigated with the use of different datasets: satellite measurements and model simulation data, and surface measurements when available (see Sect. 2).

These cities have been chosen as the focus of this study because of the availability of NH$_3$ and PM$_{2.5}$ measurements. These three cities differ in terms of the following:

1. The regulation of NH$_3$ emissions: French policies aim to reduce NH$_3$ emissions by 13 % in 2030 relative to 2005 (CITEPA, 2018) following EU ratification of the Gothenburg Protocol in 2017, whereas in Canada and Mexico there are no federal regulations for NH$_3$ emissions yet (Bittman et al., 2017).

2. Agricultural practices affecting NH$_3$ emissions differ in each region as farmers depend on meteorological conditions for fertilizer use.
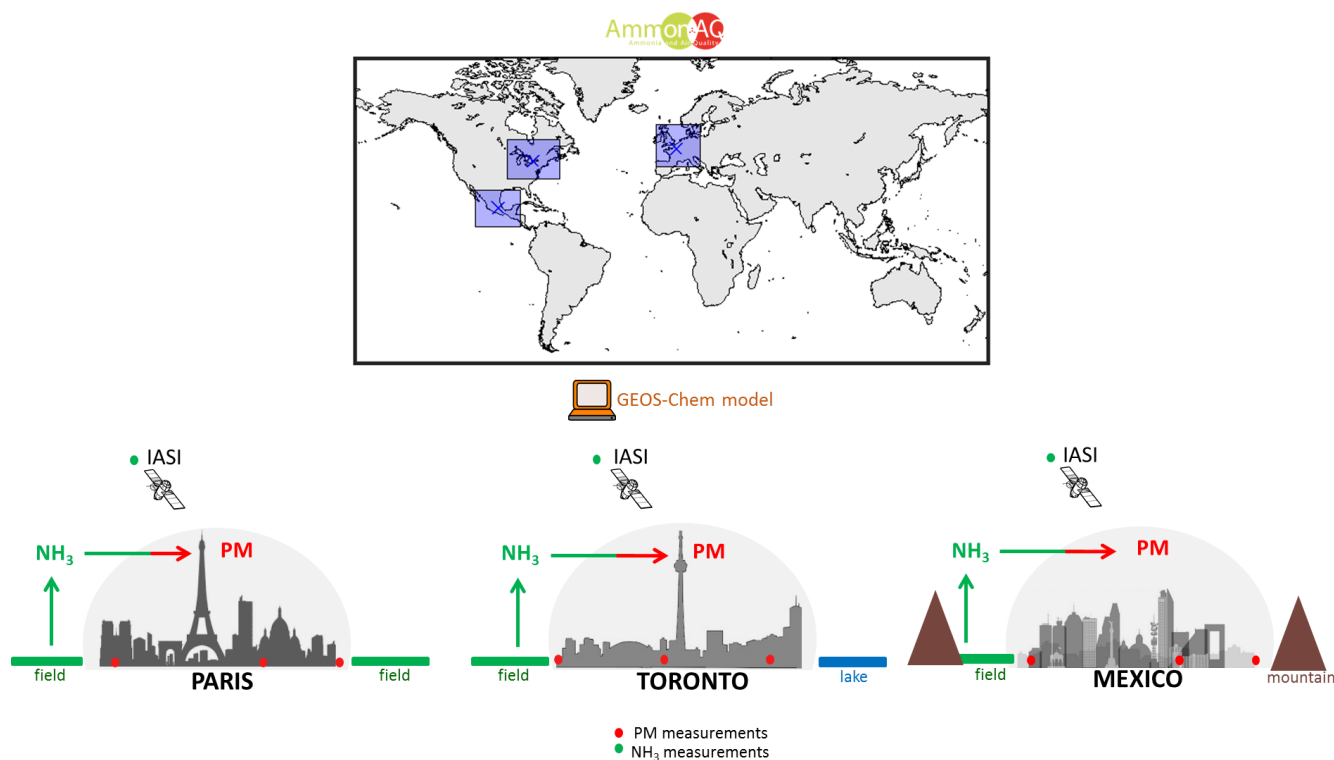
Figure 1. Representation of the AmmonAQ project. Upper panel: the three study regions investigated (in blue rectangles). Lower panel: presentation of each city and regional domain and different datasets used.

3. Meteorological and climate conditions are very different in each of the regions: drier winters and wetter summers in Toronto compared with Paris, and weak winds and strong temperature inversions in Mexico City. This influences the NH$_3$ lifetime and chemistry leading to the formation of PM$_{2.5}$.

4. Topography: Toronto is adjacent to Lake Ontario, Paris is inland, and Mexico City is a basin surrounded by mountains. This will impact the trajectories of air masses.

2 Methodology

2.1 NH$_3$ observations derived from IASI

The infrared atmospheric sounding interferometer (IASI) was launched onboard the Metop-A/B/C satellites in 2006, 2012, and 2018, respectively (Clerbaux et al., 2009). The IASI provides twice daily total column measurements of NH$_3$ globally at 09:30 and 21:30 local solar time. With its polar orbit and a swath of 2400 km, IASI pixel size is 12 km in diameter at nadir. In this work, we use version 3 of the ANNI-NH$_3$ product (Van Damme et al., 2021; Guo et al., 2021) from IASI Metop-A/B morning overpasses over the period 2008–2017 gridding a spatial resolution of 0.25° × 0.25°. The detection limit depends both on the atmospheric state

(mainly thermal contrast and NH$_3$ abundance) and the instrument characteristics. For IASI, the minimum detection limit is found to be 4–6 × 10^{15} molec. cm^{-2} (Clarisse et al., 2010).

2.2 PM$_{2.5}$ dataset derived from surface network measurements

To study local scale PM$_{2.5}$ pollution events in Paris, Toronto, and Mexico City, PM$_{2.5}$ observations of surface concentrations from 2008 to 2017 are used.

For Paris, we use hourly observations of PM$_{2.5}$ concentrations derived from 14 stations of the Airparif network (https://data-airparif-asso.opendata.arcgis.com; last access: 1 April 2022). For Toronto, we analyze hourly PM$_{2.5}$ observations derived from 11 stations supported by the Ministry of the Environment, Conservation and Parks of Ontario (http://www.airqualityontario.com; last access: 1 April 2022). For Mexico, PM$_{2.5}$ concentrations are derived from 27 stations of the Red Automática de Monitoreo Atmosférico (RAMA; http://www.aire.cdmx.gob.mx/default.php?opc=%27aKBh%27; last access: 1 April 2022) network.

All these stations are located within a 50 km radius circle of the city centers of Paris, Toronto, and Mexico City.

2.3 NH$_3$ and PM$_{2.5}$ from the GEOS-Chem model

We generate model outputs for March of 2011 because all three cities experienced both separate and combined PM$_{2.5}$ and NH$_3$ pollution events during this period. We use version 12.7.2 of the GEOS-Chem chemical transport model (Bey et al., 2001) driven by the MERRA-2 reanalysis product, including nested domains over Europe and North America at a $0.5° \times 0.625°$ horizontal resolution from which we extract modeled surface values for each city. Boundary conditions for these two nested domains are created using a global simulation for the same month at $2° \times 2.5°$ resolution. Output for the analyzed month of March includes monthly means, as well as hourly means for selected diagnostics, and is preceded by 2 months of discarded model spinup time for the global simulation, and 1 month for each nested run. Anthropogenic emissions are taken primarily from the global Community Emissions Data System (CEDS) inventory (Hoesly et al., 2018), with regional emissions from the 2011 National Emissions Inventory produced by the U.S. EPA (NEI2011) used to override global values over the United States. Biogenic non-agricultural ammonia, as well as ocean ammonia sources, are taken from the Global Emission Inventories Activities database (GEIA; Bouwman et al., 1997). Open fire emissions are generated using the GFED 4.1s inventory (Randerson et al., 2017). Sulfate–nitrate–ammonium aerosol processes are calculated using version 2.2 of the ISORROPIA thermodynamic module (Fountoukis and Nenes, 2007). Black carbon is handled as described in Wang et al. (2014), while secondary organic aerosol is produced using the simplified irreversible scheme described in Pai et al. (2020).

2.4 Back-trajectories analysis from the HYSPLIT model

To determine the effect of long-range transport affecting the local air quality of the three cities, we use the Hybrid Single-Particle Lagrangian Integrated Trajectory model (HYSPLIT; Stein et al., 2015). Note that unlike the GEOS-Chem model, HYSPLIT does not include atmospheric chemistry. For the runs, meteorological data are from the National Centers for Environmental Prediction (NCEP)and National Center for Atmospheric Research (NCAR) reanalysis at $2.5°$ global latitude–longitude projection. Note that visual inspection of the back trajectories shows that using a $2.5°$ resolution meteorological dataset is similar to using a finer meteorological dataset at $1°$ resolution (GDAS). First, we run daily 24 h back trajectories ending in the city centers at the overpass time of the IASI instrument covering the period 2008–2017. Then, for each day we calculate the mean of NH$_3$ total columns derived from IASI observations in a 50 km radius around the cities associated with each back trajectory. Finally, all back trajectories that are near each other are merged in clusters and associated with the corresponding local-scale IASI NH$_3$ concentrations.

2.5 ERA-5 meteorological data

The meteorological variables used in this study are extracted from the hourly ECMWF reanalysis (ERA5; Hersbach et al., 2020). ERA5 data are at $0.25° \times 0.25°$ resolution (native horizontal resolution of ERA5 is ~ 31 km) and are interpolated in time and space to the IASI observation. The meteorological parameters considered here are the skin temperature (T_{skin}), which is the physical temperature of the earth's surface, total precipitation (in meters of water equivalent, i.e., accumulated liquid and frozen water, comprising rain and snow), and relative humidity up to 2 m above the surface calculated from dew and air temperature at 2 m from ERA5.

3 Results

3.1 NH$_3$ source regions identification and spatiotemporal variability over the Europe, North America, and southern North America domains

Using 10 years of IASI observations, the main source regions of NH$_3$ in the three domains of study are identified (Fig. 2) and listed in Table 1. We identify 10, 9, and 19 NH$_3$ source regions over the Europe, North America, and southern North America regions, respectively. All of the sources over the Europe and North America domains are mostly related to agricultural practices (farming and spreading practices). This is in agreement with previous calculation of worldwide nitrogen inputs from fertilizer and manure (Potter et al., 2010). Around southern North America, three sources are related to fertilizer or soda ash industries (listed with C, G, and O in Fig. 2 and Table 1; Van Damme et al., 2018); the rest is agricultural.

Spatiotemporal variabilities in NH$_3$ in the atmosphere in the three regions (Fig. 2) are not expected to be similar: NH$_3$ emissions from industries in the region of southern North America are released all year long, whereas NH$_3$ emissions from agricultural practices (which are dominant over Europe and North America) depend on various surface and meteorological conditions. In order to investigate this, NH$_3$ concentrations using 10 years of IASI observations are assessed against atmospheric temperature and precipitation derived from the ERA5 reanalysis over the three domains in Fig. 3. It shows the seasonal evolution of NH$_3$ from IASI over the three regions (left panel), along with the seasonal evolution of temperature and precipitation (right panel).

For Europe and North America, NH$_3$ total columns are the highest in spring and summer. In fact, NH$_3$ concentrations over Europe exhibit two seasonal maxima in March and/or April and July and/or August (Fig. S1 in the Supplement), and in North America the maxima are in May and September (Fig. S2). This is consistent with agricultural practices (i.e., fertilizer application) and higher air temperature favoring NH$_3$ volatilization in the atmosphere.
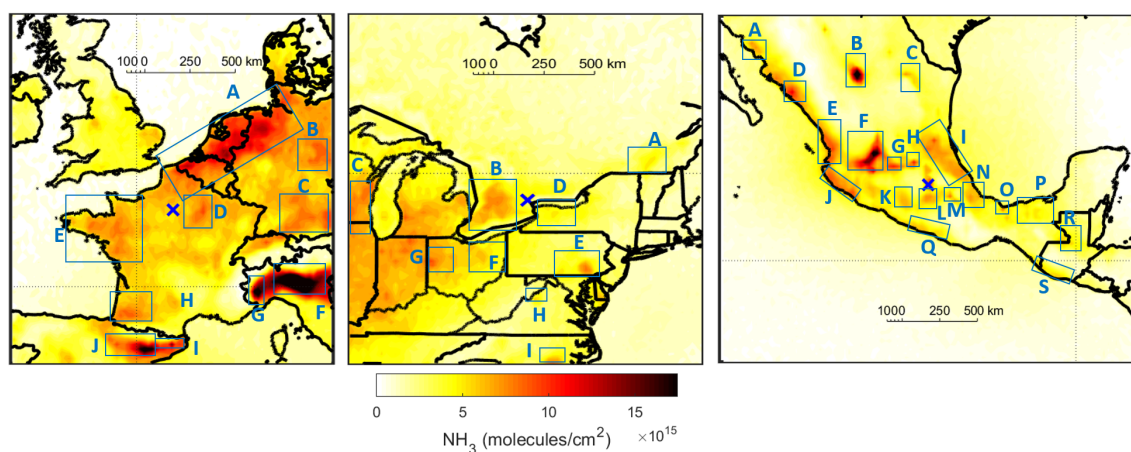
Figure 2. Source region identification of NH$_3$ derived from 10-years average of IASI total columns (molec. cm^{-2}) from 2008 to 2017. The blue crosses indicate Paris, Toronto, and Mexico City locations.

Table 1. List of NH$_3$ source regions identified using 10-years average of IASI total columns (molec. cm^{-2}) over the Europe, North America, and southern North America regions.

Europe [41–59° N; −11.25–16.25° E]		North America [35–53° N; 93.75–63.75° W]		Southern North America [9–29° N; 113.75–86.25° W]	
A	North European plain[c,d]	A	Granby (Canada)	A	Obregon (Mexico)[c]
B	Saxe Anhalt plain (Germany)	B	Elmira–Kitchener–Guelph (Canada)	B	Torreon (Mexico)[c,d]
C	Munich–Mangfall (Germany)	C	Brillion area (USA)	C	Garcia (Mexico)[b,c]
D	Champagne–Ardennes (France)	D	New York State (USA)	D	Culiacancito (Mexico)[c,d]
E	Brittany–Pays de la Loire (France)[d]	E	Lancaster County (USA)	E	Nayarit (Mexico)
F	Pô Valley (Italy)[c,d]	F	Wayne County (USA)	F	Jalostotitlan–San Juan de Los Lagos (Mexico)[c,d]
G	Valley of Piedmont (Italy)[c,d]	G	Celina–Coldwater (USA)[c]	G	Salamanca–Villagran (Mexico)[a,c]
H	Landes area (France)	H	Shenandoah Valley–Bridgewater (USA)[c]	H	Ezequiel Montes (Mexico)[c,d]
I	Vic–Manlleu (Spain)[c,d]	I	Lenoir County (USA)	I	Tampaon, Loma Alta (Mexico)[c]
J	Ebro River basin (Spain)[c,d]			J	Tecoman (Mexico)
				K	Coyuca de Catalan (Mexico)
				L	Morelos (Mexico)
				M	Tochtepec–Tehuacan (Mexico)[c]
				N	South of Veracruz (Mexico)
				O	Cosolaecaque (Mexico)[a,c]
				P	Tabasco (Mexico)
				Q	Guerrero (Mexico)
				R	Chisec (Guatemala)
				S	Texcuaco (Guatemala)

[a] Fertilizer industry; [b] soda ash industry; [c] Van Damme et al. (2018), Clarisse et al. (2019); [d] Dammers et al. (2019).

The right panel of Fig. 3 shows how temperature (red lines) and precipitation (blue bars) seasonally evolve over the three regions. In winter, atmospheric temperatures are below 5 °C in Europe and North America, and IASI observations reveal almost no NH$_3$ hot spots (Fig. 3, left panel). This can be due to the lack of NH$_3$ abundance, lower volatilization in this temperature range, no agricultural emissions in winter, and/or the reduced sensitivity of the IASI NH$_3$ retrievals in winter (Van Damme et al., 2017). The high value over Canada and the Arctic in winter can be associated with high
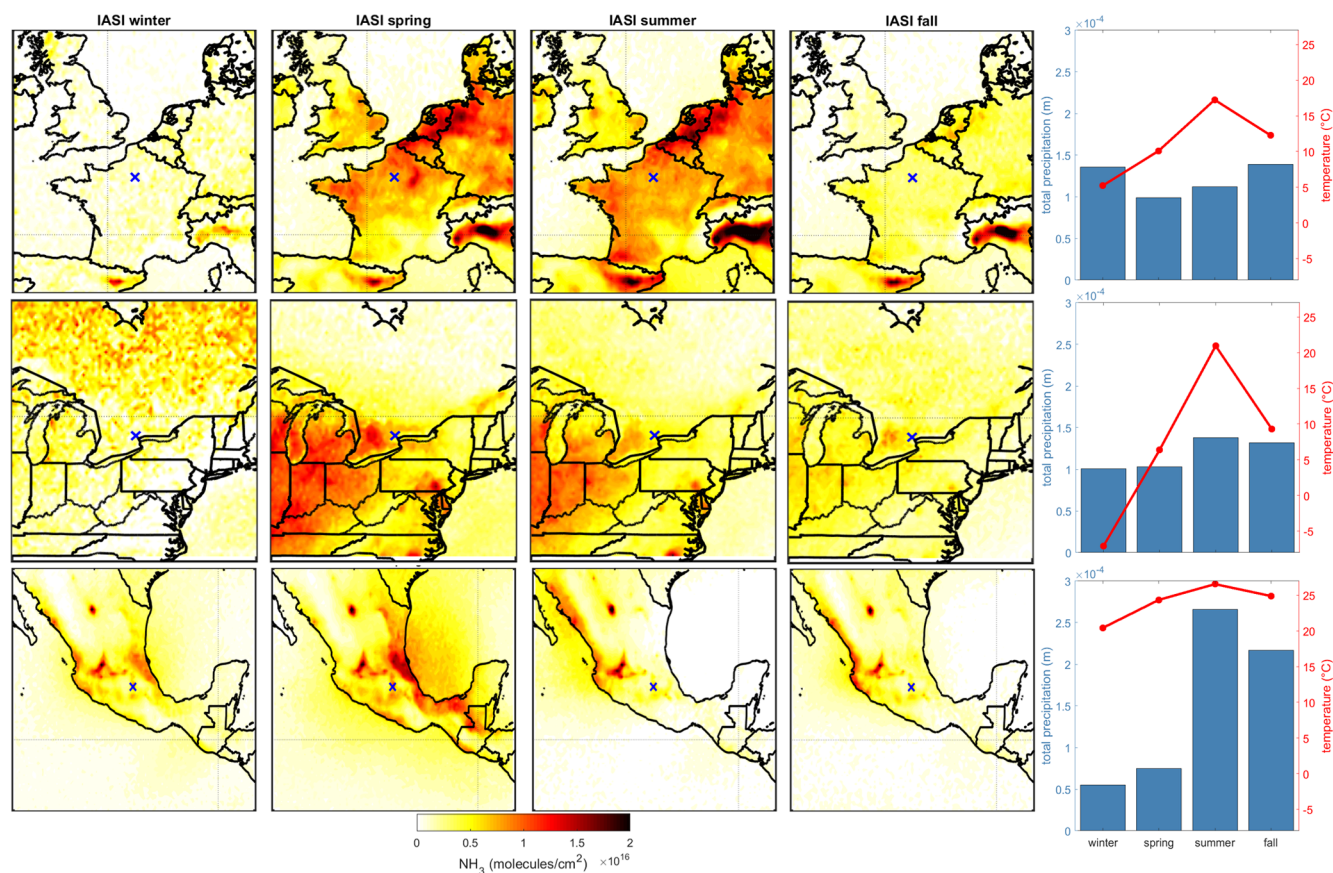
Figure 3. Seasonal maps of NH$_3$ total columns (molec. cm^{-2}) derived from 10 years (2008–2017) of IASI observations, along with seasonal means of atmospheric temperature (red line) and precipitation (blue bar chart) over the Europe (upper panels), North America (middle panels), and southern North America (lower panels) regions.

uncertainties in the NH$_3$ retrievals due to low thermal contrast.

In southern North America, NH$_3$ seasonal variations are less pronounced than in the other two regions. Figure 3 shows that the NH$_3$ concentrations over several sources, such as Torreon and San Juan de Los Lagos (Fig. 2, right panel, boxes B and F), are high during all seasons, which could be associated with the weak seasonal cycle of temperature in this region closer to the Equator.

In spring, seasonal precipitations are the lowest for the three regions. This is reflected in the high NH$_3$ concentrations in the left panel. Over Europe and North America, this can be related to the agricultural spreading practices period and higher atmospheric temperature favoring NH$_3$ volatilization. In southern North America, NH$_3$ concentrations observed by IASI are the highest in spring when atmospheric temperatures are high and precipitation rates are low. In addition, biomass burning, which is often encountered during this period, could explain higher atmospheric NH$_3$ concentrations in spring. NH$_3$ reach maximum values in April and/or May (Fig. S3) just before the start of the rainy season, potentially reducing observed NH$_3$ concentrations due to the wet deposition of atmospheric gaseous ammonia (Asman et al., 1998).

Since in Europe and North America NH$_3$ sources are mostly agriculture related (with small contributions from industries), the temperature and NH$_3$ relationship is expected to be relatively easy to interpret: when the land surface temperature increases, volatilization of ammonia from the fertilized and manured soil is favored, and atmospheric ammonia increases. The corresponding determination factors r^2 for this relationship in Europe and North America are 0.85 and 0.80, respectively (polynomial fit of second order). This is not the case in southern North America, in which some of the ammonia sources are also industrial and they contribute greatly to the atmospheric NH$_3$: the concentrations of ammonia are therefore not directly temperature dependent, as we can see in Fig. S4 in the right upper panel in ($r^2 = 0.46$). There is nonetheless a relationship in southern North America that is due to the fact that we have constant high ammonia sources and temperatures (Fig. 3). In fact, the relationships between NH$_3$ and temperature, on one hand, and precipitation and relative humidity, on the other hand, are not linear;

this has been equally shown in a previous study (Sutton et al., 2013).

To further investigate the temperature and NH$_3$ relationship, we show in Fig. 4 the evolution of NH$_3$ with respect to land surface temperature over different subregions of the Europe domain (listed in Table 1). Similar graphics for the North America and southern North America domains are shown in Figs. S5 and S6. We observe a peak of NH$_3$ followed by a local maximum plateau between 10 and 25 °C approximately in all of the regions of the Europe domain (Fig. 4). In fact, the NH$_3$ detected in this range of temperature can indicate the fertilizer application period, since most of them (up to 80 %) were detected during the spring and fall seasons. For instance, over the Po Valley (Table 1, region F; Fig. 4), 36 % of the NH$_3$ detected in the bins 10–25 °C correspond to the spring season, whereas 35 % correspond to the fall season (not shown). In Celina–Coldwater (Table 1, region G), 82 % of the NH$_3$ detected between 10 and 25 °C corresponds to the spring and fall seasons, and the percentage is split equally (Fig. S5).

We choose to show the subregions in the vicinity of the Europe domain, since they are mostly agricultural sources. The "bumps" corresponding to the fertilizer application are very clear in all of the subregions. This bump was detected to a lower extent for agricultural regions affecting North America (Fig. S5). Over the agricultural regions in the southern North America domain, the bumps are clear in the regions A–D (Fig. S6a). When the seasonal temperatures do not fluctuate during the fertilizer application, any increase in atmospheric NH$_3$ is due to the sudden addition of nitrogen fertilizers to the soil. In southern North America, the regions E–M show that the highest NH$_3$ concentrations were observed as the temperature increased during the growing seasons (Fig. S6). A possible explanation to the resemblance among the regions A–D is that they share similar climate properties (Steppe and Desert), unlike the rest of the subregions in the same domain (tropical and/or subtropical). Since the temperatures in the Europe and southern North America domains are higher (Fig. 3, right panels) in the spring and fall seasons (fertilizer application period) than those in North America, this bump is clearer in the latter. The bumps seen for the Europe regional domain are clearer than those of southern North America, possibly related to the fact that in autumn in Europe precipitation is lower than those in southern North America, leading to lower NH$_3$ loss through wet deposition.

3.2 NH$_3$ budget over Paris, Toronto, and Mexico City

Temperature, relative humidity, and precipitation are not the only factors affecting the NH$_3$ concentrations. In order to analyze the impact of long-range transport on NH$_3$ concentrations measured over (and not domains) of Paris, Toronto, and Mexico City, HYSPLIT back trajectories have been used. For each day of IASI NH$_3$ observations made in a 50 km radius circle from the city center, a 24 h back trajectory

has been performed from 2008 to 2017. There are between 3643 and 4008 back trajectories for Paris, Toronto, and Mexico City. Then, a seven-cluster analysis has been applied to these datasets and NH$_3$ mean concentrations measured inside the cities by IASI have been allocated to the different mean cluster trajectories according to the corresponding back trajectories. Details about this analysis are described in Fig. S7. The result is shown in Fig. 5.

For Paris, 25 % of all back trajectories (875) that are associated with the highest NH$_3$ concentrations, i.e., 4.71 × 10^{15} molec. cm^{-2} on average, originate from the surrounding south regions (Fig. 5, black line). Clusters 2 and 3 are also associated with high NH$_3$ concentrations and come from the north/northeast. This is consistent with previous analyses using HYSPLIT (Viatte et al., 2020) and FLEXPART models (Viatte et al., 2021). As expected, the back trajectories coming from the ocean are related with almost no NH$_3$ concentrations (left panel, light and dark blue lines).

Over Toronto, the highest NH$_3$ concentrations (24 % and 14 %) measured in the city are allocated to long-range transport located south/southwest (Fig. 5, middle panel, black and purple lines) coming from the United States where most of the feedlots are. Of NH$_3$ concentrations, 9 %–17 % come from the west and the east of Toronto (clusters 3–5) where atmospheric NH$_3$ has increased in the past decade possibly due to the reduced chemical loss of atmospheric NH$_3$ to form particulate NH$_4^+$ (Fig. 2, boxes A and B; Yao and Zhang, 2019). The two back-trajectory clusters that are related to low NH$_3$ concentrations come from the north (Fig. 5, light and dark blue lines) where no NH$_3$ sources have been identified.

In the southern North America domain, back trajectories come from relatively close regions since orographic conditions around Mexico City limit long-range transport. In this city, as shown in the right panel of Fig. 5, the highest NH$_3$ concentrations are associated with air masses coming from the southwest (11 %, black line; 22 %, purple line) and southeast (27 %, red line). Air parcels coming from the north are associated with relatively low NH$_3$ concentrations measured in Mexico City.

3.3 Pollution events over Paris, Toronto, and Mexico City from 2008 to 2017

After assessing the NH$_3$ distribution under average climate conditions, we focus now on pollution events occurring at the three cities. These events are identified by applying the Fourier series of order 3 (Yamanouchi et al., 2021; Herrera et al., 2022) on the surface PM$_{2.5}$ and satellite NH$_3$ observations at the city scale (i.e., 50 km radius circle from the city centers). The Fourier fit accounts for the "natural" variability (seasonality) in the time series and helps identify pollution events that are 2 standard deviations above this natural variability. It is a robust method commonly used to quantify trends and identify enhancements in long-term time series (Zellweger et al., 2009). Pollution events occurrence per city
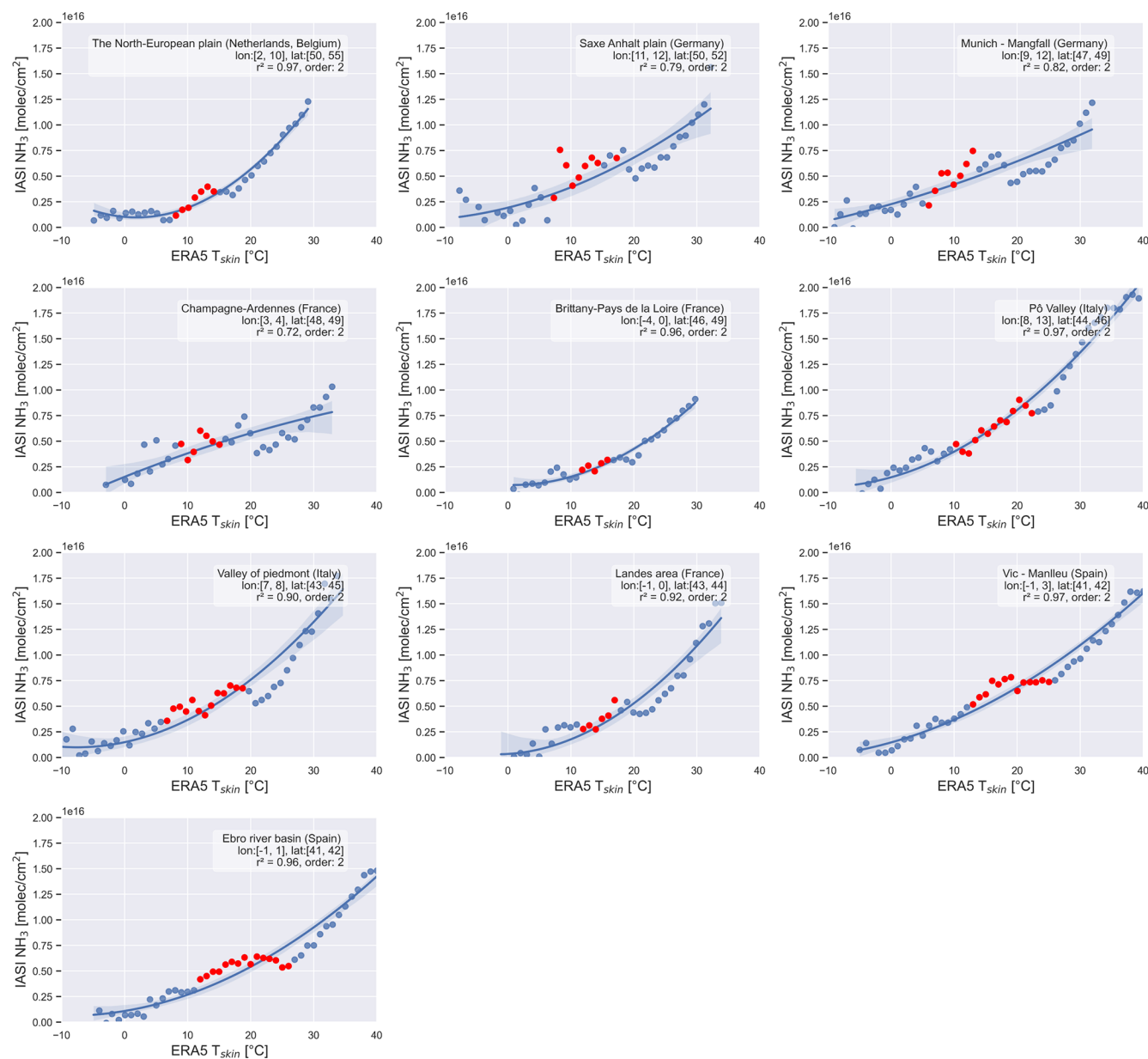
Figure 4. Yearly IASI NH$_3$ total columns (molec. cm^{-2}) averaged per bins of ERA5 skin temperatures ($^\circ$C), with an interval of 1 $^\circ$C between each consecutive bin. The red circles denote the growing seasons, in which at least 60 % of the NH$_3$ is detected during the March–May and September–November periods. See Fig. 2 and Table 1 for the localization of the subregions around Europe.

per year and per season are shown in Fig. 6a and b, respectively.

The figure shows that NH$_3$ pollution episodes are found to be annually frequent in the three cities. In Toronto and Mexico City, PM$_{2.5}$ pollution events are encountered annually (with higher numbers in Mexico City), whereas no events are detected in 2009, 2015, and 2017 in Paris.

Numbers of identified days of PM$_{2.5}$ pollution events are 88, 58, and 50 in Mexico City, Toronto, and Paris, respectively. For NH$_3$ pollution events, they occur more in Toronto than in Mexico City and Paris, with number of days of 94,

73, and 56, respectively. Common days of high NH$_3$ and PM$_{2.5}$ concentrations are found in all three cities, especially in spring (Fig. 6b), coinciding with the high seasonal NH$_3$ concentrations shown in Fig. 3.

To further investigate the impact of transport on pollution events occurring in the three cities, we have analyzed the wind fields patterns for different cases: (i) the whole dataset (i.e., ensemble 2008–2017), (ii) days of NH$_3$ and PM$_{2.5}$ pollution events occurring separately, and (iii) days when high concentrations for both are observed. Figure 7 shows wind roses computed for the ensemble and these different types of
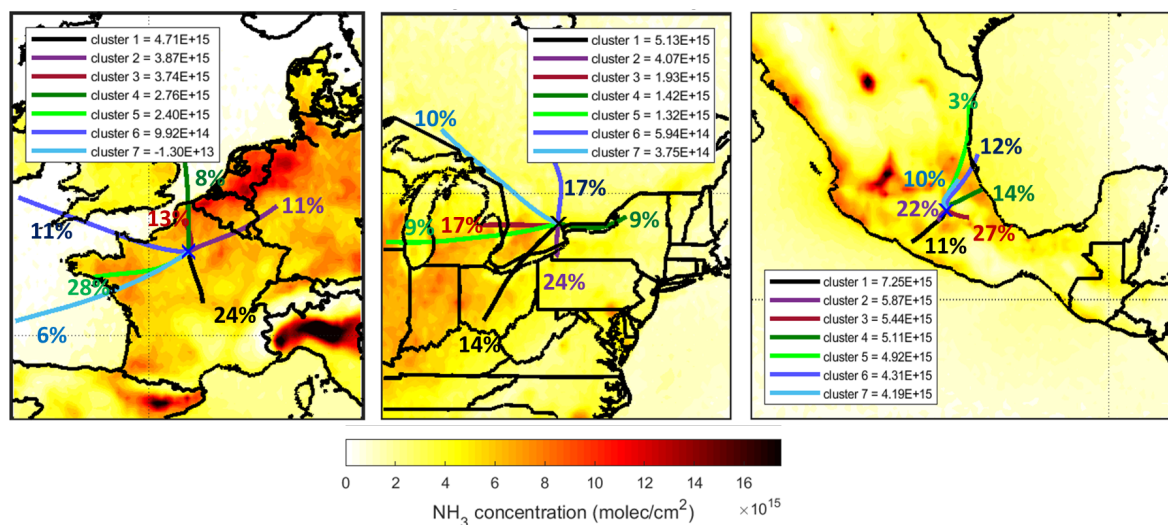
Figure 5. Seven cluster–mean backward trajectories over the Europe, North America, and southern North America regions for the whole time period between 2008 and 2017. Back trajectories are color coded in function of the corresponding NH$_3$ concentrations measured inside the cities. The numbers indicate the percentage of trajectories allocated to a cluster.
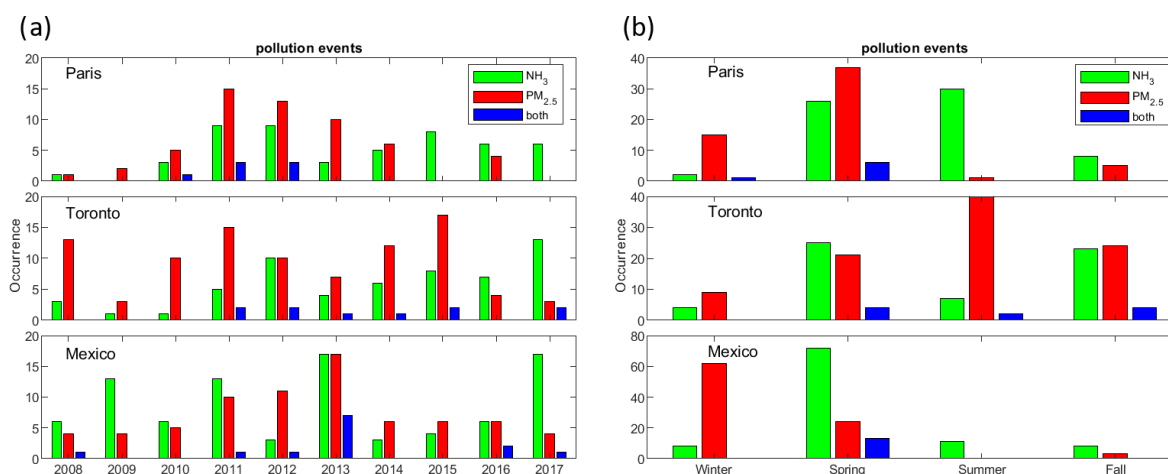

Figure 6. Annual **(a)** and seasonal **(b)** occurrence of pollution events of NH$_3$ (green bars), PM$_{2.5}$ (red bars), and NH$_3$ and PM$_{2.5}$ simultaneously (blue bars) detected from 2008 to 2017 in Paris (upper panel), Toronto (middle panel), and Mexico City (lower panel).

pollution events (i.e., PM$_{2.5}$, NH$_3$, and both occurring during the same day). The radial distance in the wind roses indicates the frequency of the wind direction occurrence. In general, wind speed is lower in Mexico City (max 3 m s^{-1}) compared with Toronto and Paris (up to 10 m s^{-1}) because of the mountainous topography that blocks and slows air masses exchange in Mexico.

In Paris, the ensemble wind roses show a dominant northeast/southwest pattern. NH$_3$ pollution events are associated with wind coming from various directions at all wind speeds, which was suggested by the HYSPLIT cluster analysis (Fig. 5), whereas PM$_{2.5}$ events are present mainly under high northeast wind. When both NH$_3$ and PM$_{2.5}$ high concentrations are observed in Paris, the wind field can have two

patterns: low wind speed coming from all directions (except the south) or high wind speed coming from the northeast. This confirms the importance of transport of NH$_3$ and PM$_{2.5}$ from the northeast and could suggest the interconversion of PM$_{2.5}$ to NH$_3$ at low wind speed.

In Toronto, the ensemble show that dominant wind pattern is coming from the south. For all the pollution events (NH$_3$, PM$_{2.5}$, and both) the wind is coming from the southwest, confirming the long-range transport of pollutants from the United States.

In Mexico City, the dominant pattern (ensemble) is southwest/northeast wind fields. For days of NH$_3$ pollution events, wind mainly comes from the south/southwest, and for PM$_{2.5}$, wind comes from all directions with a significant northeast
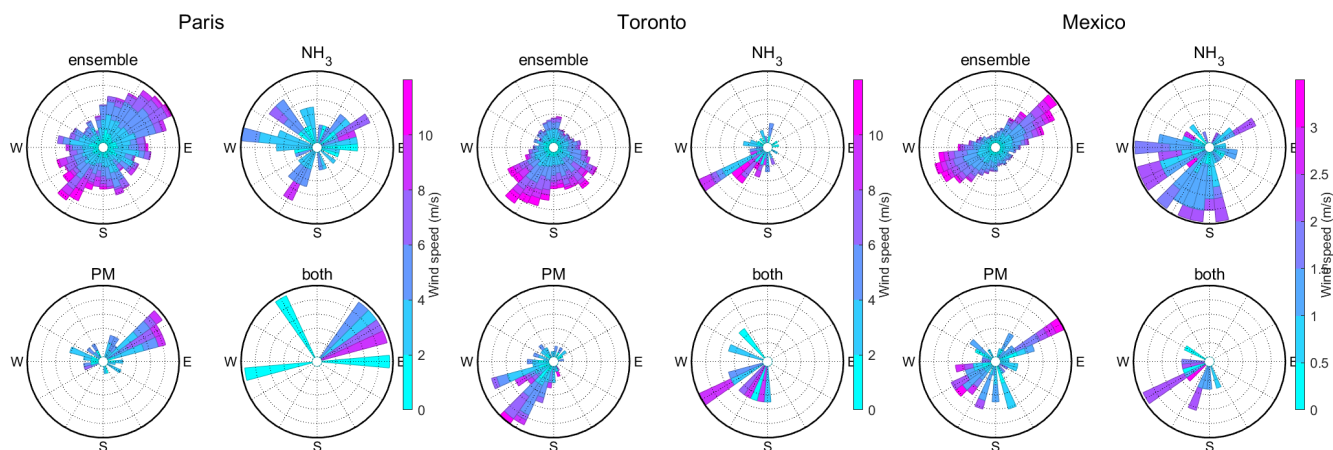
Figure 7. Wind roses corresponding to the ensemble of all observations, the NH$_3$, PM$_{2.5}$, and both NH$_3$ and PM$_{2.5}$ simultaneous pollution events, derived from 2008 to 2017 over Paris (left panels), Toronto (middle panels), and Mexico City (right panels).

wind pattern. Days of both pollution events are associated with wind coming from the west/southwest only.

3.4 Case study: NH$_3$ and PM$_{2.5}$ concentrations comparison with the GEOS-Chem model in March 2011

The occurrence of pollution events varies from year to year (Fig. 6). However, in 2011, all three cities experienced PM$_{2.5}$ and NH$_3$ separate and combined pollution events. For this reason, GEOS-Chem model simulations were performed in March 2011 to interpret the events and evaluate the model performance.

Spatial and temporal coincidence criteria have been applied to GEOS-Chem outputs to compare with IASI morning observations. For example, model outputs between 08:30 and 11:30 UTC coincident with IASI overpasses have been selected, and only collocated model outputs (at $0.5° × 0.625°$ horizontal resolution) have been selected coincident with IASI observations. Averages of numbers of coincident observations are 1324, 1138, and 3000 over the Europe, North America, and southern North America domains of study during March 2011.

Figure 8 shows the 1-month comparison between the two datasets. Over the regional domains, the coefficient of correlation between daily model NH$_3$ concentrations and IASI NH$_3$ observations are $R = 0.50$, $R = 0.55$, and $R = 0.33$, over Europe, North America, and southern North America, respectively, with related p values < 0.01. NH$_3$ columns derived from the GEOS-Chem model are overall underestimated with mean relative difference (MRD = (model − observations)/observations) of -37%, -31%, and -2% over Europe, North America, and southern North America, respectively.

Over Europe and North America, IASI and GEOS-Chem capture some of the same pollution events (on 12, 15, and
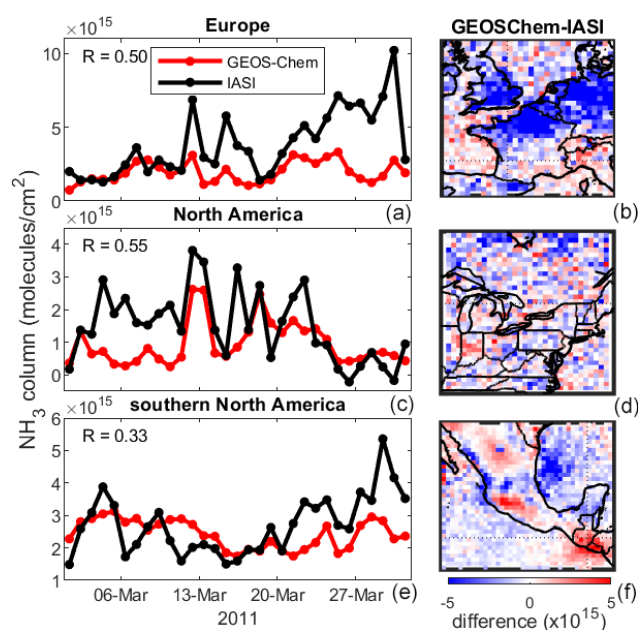

Figure 8. (a, c, e) Time series of daily NH$_3$ columns derived from IASI (black lines) and the GEOS-Chem model (red lines) over Europe (a), North America (c), and southern North America (e). (b, d, f) Maps of NH$_3$ columns (in molec. cm^{-2}) differences between IASI and GEOS-Chem model (model observations) for March 2011.

30 March over Europe, and 12, 13, and 18 March over North America). In southern North America, the underestimation of the GEOS-Chem NH$_3$ columns is less pronounced (MRD is -2%) than in the other regions, but the day-to-day variability is not well represented in the model.

The GEOS-Chem model NH$_3$ total columns are lower than those from IASI in March 2011 over specific locations in the southern North America and Europe domains (Fig. 8b, d, f). For the Europe region, GEOS-Chem NH$_3$ columns are

smaller than the IASI ones over the north of France, Belgium, the Netherlands, north of Spain (in particular sources A–E, I, and J of Fig. 2) and the United Kingdom. For the southern North America domain, GEOS-Chem NH$_3$ columns are smaller than the IASI ones over the western Mexican coast (sources A, D, E, and J of Fig. 2 and Table 1), central (sources F, G, and H of Fig. 2) and southeastern (sources O and P of Fig. 2) Mexico City, and over the Pacific Ocean, whereas they are higher in Guatemala (sources S and R of Fig. 2) and west of Mexico City.

Over the North America domain, spatial distribution of the differences between NH$_3$ columns derived from GEOS-Chem and IASI are less pronounced than in the Europe and southern North America domains. IASI NH$_3$ columns are smaller than GEOS-Chem outputs over the southern United States and over Lancaster County, Pennsylvania (sources E and I of Fig. 2), and higher over Indiana (both in the United States).

At the city scale of Paris and Mexico City, the daily model NH$_3$ columns are in relatively good agreement with IASI observations within a 50 km radius circle from the city centers (not shown here), since the coefficients of correlation are $R = 0.42$ and $R = 0.52$, respectively. Similar to the regional domains, GEOS-Chem NH$_3$ columns are relatively underestimated at the city scale of Paris and Mexico City, with an MRD of -108% and -28%. At the city scale of Toronto, the correlation between the NH$_3$ columns derived from the model and observed by IASI is poor, with a coefficient of correlation of $R = -0.32$, and a small underestimation of the modeled NH$_3$ concentrations is found with an MRD of -6%.

Local comparison of PM$_{2.5}$ concentrations at the city scale (over Paris, Toronto, and Mexico) is shown in Fig. 9a, c, and e, which show that PM$_{2.5}$ concentrations calculated by the model in March 2011 are in relatively better agreement with the surface observations with $R = 0.63$, $R = 0.43$, and $R = 0.54$ in Paris, Toronto, and Mexico City. In Paris and Mexico City, PM$_{2.5}$ concentration values derived from the observations are overall higher than the GOES-Chem concentrations with MRD values of -13% and -20%, respectively, whereas GEOS-Chem PM$_{2.5}$ concentrations are higher than those in the observations in Toronto with an MRD value of 519%.

Figure 9b, d, and f show the chemical composition of the PM$_{2.5}$ from GEOS-Chem and inform us about the different pollution sources. Organic matter sources are split equally between the primary emissions and the oxidation of volatile organic compounds (Day et al., 2015). The SNA (sum of sulfate, nitrate, and ammonium) sources originate in chemical transformation of gaseous precursors in the atmosphere, whereas black carbon comes from primary emissions of industrial and traffic combustion.

According to the GEOS-Chem model, SNA dominates the PM$_{2.5}$ chemical composition mass in March 2011 over the three cities, meaning that the dominant source of PM$_{2.5}$ mass comes from the secondary oxidation path. This partition of SNA in March 2011 from the model is higher than what has been reported based on 1-year measurements performed in 2013: 43 %, 42 %, and 33 % of the PM$_{2.5}$ mass composition in Paris, Toronto, and Mexico City, respectively (Cheng et al., 2016).

In Paris, the March 2011 pollution episode has been analyzed in terms of geographical origins and aerosol properties (Chazette and Royer, 2017) but not in terms of aerosol speciation.

Comparing the GEOS-Chem outputs used in this study with 2 years of observations of aerosol chemical composition in Paris (2011–2013) (Petit et al., 2015), we found that the sulfate component is slightly higher in the GEOS-Chem model than in the springtime observations (21 % compared with 11 %), whereas modeled organic carbon is lower than the observations (8 % compared with 33 %). This springtime underestimation of organics in atmospheric models has previously been reported in Paris (Sciare et al., 2010; Petit et al., 2015; Lanzafame et al., 2021) and could be associated with an underestimation of the organic matter emissions from residential contributions (Denier van der Gon et al., 2015). Regarding the secondary aerosol, observations in Paris during the March 2015 pollution event show that it accounts for more than 50 % of the PM concentration (Petit et al., 2017), which is in agreement with the SNA partition in our GEOS-Chem model simulation.

In Toronto, PM$_{2.5}$ speciation is monitored by the National Air Pollution Surveillance Program (NAPS; https://www.canada.ca/en/environment-climate-change/services/air-pollution/monitoring-networks-data/national-air-pollution-program.html, last access: 29 September 2022) network. Observations in March 2011 reveal that inorganic nitrate burden is overestimated by a factor of 2 in the GEOS-Chem run (41 % in the model compared with 20 % in the observations), whereas sulfate and black carbon abundances are underestimated by a factor of 2 (15 % and 6 % in the model compared with 27 % and 12 % in the observations).

In Mexico City, the organic matter represents the most abundant fraction of the aerosol, which is consistent with measurements made during several campaigns performed in the dry season of 2006 during the Megacity Initiative: Local And Global Research Observations (MILAGRO; Molina et al., 2010; Karydis et al., 2011) and Aerosoles en Ciudad Universitaria (ACU) in 2015 (Salcedo et al., 2018). Observations performed during the dry and warm season of 2019 reported that SNA correspond to 30 % of the aerosol mass concentration (Retama et al., 2022), which is consistent with what has been reported before (Cheng et al., 2016) and the chemical composition modeled in our study. The organic fraction is found to be dominant in the observations (Retama et al., 2022) as suggested in the GEOS-Chem model over Mexico City. Daily cycles appear exaggerated in the model with maxima well represented and minima greatly underes-
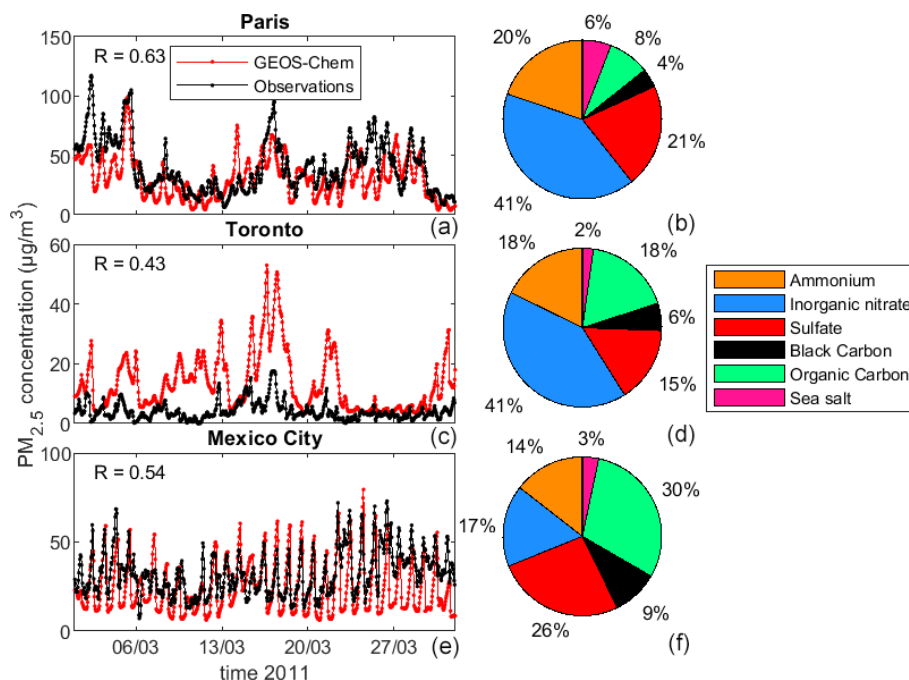
Figure 9. (a, c, e) Time series of hourly PM$_{2.5}$ (µg m^{-3}) derived from surface observations (black lines) and the GEOS-Chem model (red lines) over Paris **(a)**, Toronto **(c)**, and Mexico City**(e)** for March 2011. **(b, d, f)** PM$_{2.5}$ speciation (% in total mass) derived from the GEOS-Chem run for March 2011.

timated. This could suggest model issues in terms of atmospheric dynamics (removal and transport or planetary boundary layer dynamics) due to coarseness of grid.

4 Conclusion

The AmmonAQ project aims to determine the impact of intensive agricultural practices on urban pollution in the Paris, Toronto, and Mexico metropolitan areas. For this purpose, PM$_{2.5}$ and NH$_3$ measurements from in situ instruments and satellite infrared spectrometers, and atmospheric model simulations, have been combined.

Using 10 years of IASI observations, NH$_3$ source regions have been identified. All of the sources are from the agricultural sector (husbandry and fertilizer application) in the Europe and North America domains, whereas some of them are industrial in the southern North America region. Consequently, the spatiotemporal variability of NH$_3$ is different, with stronger seasonal variabilities in Europe and North America. A strong correlation is found between NH$_3$ total columns and surface temperature (T_{skin}) for all regions, with higher correlation over agricultural regions, and when the temperature seasonal cycle is pronounced. We find that the timing of the fertilizer application can be detected through local maxima in the NH$_3$ and T_{skin} relationship curve.

According to HYSPLIT cluster analysis, the highest NH$_3$ concentrations measured at the city scale are associated with air masses coming from the surrounding regions: the

north/northeast of Paris, the south/southwest of Toronto, and the southeast/southwest of Mexico City. These air masses lead to the exacerbation of the degradation of air quality in each of the three cities.

Pollution episodes are found to be annually frequent at the three cities, especially in spring when high NH$_3$ and PM$_{2.5}$ are observed. In Paris and Mexico pollution is transported along the northeast/southwest line, whereas in Toronto the transboundary transport of pollutants from the United States is dominant during pollution events.

The evaluation of the GEOS-Chem outputs in March 2011 reveals that NH$_3$ concentrations are overall underestimated by the model at the regional scale, with, however, a good representability of the day-to-day variability in Europe and North America domains. NH$_3$ columns derived from IASI and the GEOS-Chem model exhibit substantial spatial differences in the Europe and southern North America areas. In terms of PM$_{2.5}$ concentrations at the city scale, we show that they are underestimated in Paris and Mexico City but overestimated in Toronto.

The IASI thermal infrared remote sensors have proved to be valuable to monitor pollution events over cities. The main limitations are associated with the low revisit time (at the beginning and end of the day), the lack of sensitivity to the surface in particular in winter, and the fact that some areas are not well covered during cloudy scenes. In the near future the next generation of instruments will have improved capabilities to sound deeper in the atmosphere (Crevoisier

et al., 2014). The IRS-MTG satellite instrument that should be launched in 2024 in geostationary orbit will offer the capacity to enhance this research over Europe thanks to better temporal (measurements every 30–45 min) and spatial (4 km × 4 km pixel) resolution.

References

Abeed, R., Clerbaux, C., Clarisse, L., Van Damme, M., Coheur, P.-F., Safieddine, S.: A space view of agricultural and industrial changes during the Syrian civil war, Elementa, 9, 000041, https://doi.org/10.1525/elementa.2021.000041, 2021.

Airparif: Les données ouvertes de qualité de l'air en Île-de-France, Airparif [data set], https://data-airparif-asso.opendata.arcgis.com/, last access: 29 September 2022.

Asman, W., Sutton, M. A., and Schjørring, J. K.: Ammonia: emission, atmospheric transport and deposition, New Phytol., 139, 27–48, 1998.

Behera, S. N., Betha, R., and Balasubramanian, R.: Insights into Chemical Coupling among Acidic Gases, Ammonia and Secondary Inorganic Aerosols, Aerosol Air Qual. Res., 13, 1282–1296, https://doi.org/10.4209/aaqr.2012.11.0328, 2013.

Bey, I., Jacob, D. J., Yantosca, R. M., Logan, J. A., Field, B. D., Fiore, A. M., Li, Q., Liu, H. Y., Mickley, L. J., and Schultz, M. G.: Global modeling of tropospheric chemistry with assimilated meteorology: Model description and evaluation, J. Geophys. Res.-Atmos., 106, 23073–23095, https://doi.org/10.1029/2001JD000807, 2001.

Bittman, S., Sheppard, S. C., and Hunt, D.: Potential for mitigating atmospheric ammonia in Canada, Soil Use Manage, 33, 263–275, https://doi.org/10.1111/sum.12336, 2017.

Bouwman, A. F., Lee, D. S., Asman, W. A. H., Dentener, F. J., Van Der Hoek, K. W., and Olivier, J. G. J.: A global high-resolution emission inventory for ammonia, Global Biogeochem. Cy., 11, 561–587, https://doi.org/10.1029/97GB02266, 1997.

Bressi, M., Sciare, J., Ghersi, V., Mihalopoulos, N., Petit, J.-E., Nicolas, J. B., Moukhtar, S., Rosso, A., Féron, A., Bonnaire, N., Poulakis, E., and Theodosi, C.: Sources and geographical origins of fine aerosols in Paris (France), Atmos. Chem. Phys., 14, 8813–8839, https://doi.org/10.5194/acp-14-8813-2014, 2014.

Chazette, P. and Royer, P.: Springtime major pollution events by aerosol over Paris Area: From a case study to a multiannual analysis, J. Geophys. Res.-Atmos., 122, 8101–8119, https://doi.org/10.1002/2017JD026713, 2017.

Cheng, Z., Luo, L., Wang, S., Wang, Y., Sharma, S., Shimadera, H., Wang, X., Bressi, M., de Miranda, R. M., Jiang, J., Zhou, W., Fajardo, O., Yan, N., and Hao, J.: Status and characteristics of ambient PM$_{2.5}$ pollution in global megacities, Environ. Int., 89–90, 212–221, https://doi.org/10.1016/j.envint.2016.02.003, 2016.

Clarisse, L., Shephard, M. W., Dentener, F., Hurtmans, D., Cady-Pereira, K., Karagulian, F., Van Damme, M., Clerbaux, C., and Coheur, P.-F.: Satellite monitoring of ammonia: A case study of the San Joaquin Valley, J. Geophys. Res., 115, D13302, https://doi.org/10.1029/2009JD013291, 2010.

Clarisse, L., Van Damme, M., Clerbaux, C., and Coheur, P.-F.: Tracking down global NH$_3$ point sources with wind-

adjusted superresolution, Atmos. Meas. Tech., 12, 5457–5473, https://doi.org/10.5194/amt-12-5457-2019, 2019.

Clerbaux, C., Boynard, A., Clarisse, L., George, M., Hadji-Lazaro, J., Herbin, H., Hurtmans, D., Pommier, M., Razavi, A., Turquety, S., Wespes, C., and Coheur, P.-F.: Monitoring of atmospheric composition using the thermal infrared IASI/MetOp sounder, Atmos. Chem. Phys., 9, 6041–6054, https://doi.org/10.5194/acp-9-6041-2009, 2009.

CITEPA: Inventaire des émissions de polluants atmosphériques en France métropolitaine, format CEE-NU, Référence CITEPA no. 1505NFR/2018|UNECE_France_mars2018_encours.docx, https://cibe.fr/wp-content/uploads/2018/08/2018-CITEPA-Inventaire-émissions-polluants.pdf (last access: 29 September 2022), 2018.

Crevoisier, C., Clerbaux, C., Guidard, V., Phulpin, T., Armante, R., Barret, B., Camy-Peyret, C., Chaboureau, J.-P., Coheur, P.-F., Crépeau, L., Dufour, G., Labonnote, L., Lavanant, L., Hadji-Lazaro, J., Herbin, H., Jacquinet-Husson, N., Payan, S., Péquignot, E., Pierangelo, C., Sellitto, P., and Stubenrauch, C.: Towards IASI-New Generation (IASI-NG): impact of improved spectral resolution and radiometric noise on the retrieval of thermodynamic, chemistry and climate variables, Atmos. Meas. Tech., 7, 4367–4385, https://doi.org/10.5194/amt-7-4367-2014, 2014.

Dammers, E., McLinden, C. A., Griffin, D., Shephard, M. W., Van Der Graaf, S., Lutsch, E., Schaap, M., Gainairu-Matz, Y., Fioletov, V., Van Damme, M., Whitburn, S., Clarisse, L., Cady-Pereira, K., Clerbaux, C., Coheur, P. F., and Erisman, J. W.: NH$_3$ emissions from large point sources derived from CrIS and IASI satellite observations, Atmos. Chem. Phys., 19, 12261–12293, https://doi.org/10.5194/acp-19-12261-2019, 2019.

Day, M. C., Zhang, M., and Pandis, S. N.: Evaluation of the ability of the EC tracer method to estimate secondary organic carbon, Atmos. Environ., 112, 317–325, https://doi.org/10.1016/j.atmosenv.2015.04.044, 2015.

Denier van der Gon, H. A. C., Bergström, R., Fountoukis, C., Johansson, C., Pandis, S. N., Simpson, D., and Visschedijk, A. J. H.: Particulate emissions from residential wood combustion in Europe – revised estimates and an evaluation, Atmos. Chem. Phys., 15, 6503–6519, https://doi.org/10.5194/acp-15-6503-2015, 2015.

ECCC (Environment and Climate Change Canada): Canadian Environmental Sustainability Indicators: Air pollutant emissions, Consulted on Month day, year, https://www.canada.ca/en/environment-climate-change/services/environmental-indicators/air-pollutant-emissions.html, last access: 29 September 2022.

Fountoukis, C. and Nenes, A.: ISORROPIA II: a computationally efficient thermodynamic equilibrium model for K$^+$-Ca^{2+}-Mg^{2+}-NH$_4^+$-Na$^+$-SO$_4^{2-}$-NO$_3^-$-Cl$^-$-H$_2$O aerosols, Atmos. Chem. Phys., 7, 4639–4659, https://doi.org/10.5194/acp-7-4639-2007, 2007.

Gobierno de la ciudad de México: Bases de datos – Red Automática de Monitoreo Atmosférico (RAMA), Gobierno de la ciudad de México [data set], last access: 29 September 2022.

Guo, X., Wang, R., Pan, D., Zondlo, M. A., Clarisse, L., Van Damme, M., Whitburn, S., Coheur, P.-F., Clerbaux, C., Franco, B., Golston, L. M., Wendt, L., Sun, K., Tao, L., Miller, D., Mikoviny, T., Müller, M., Wisthaler, A., Tevlin, A. G., Murphy, J. G., Nowak, J. B., Roscioli, J. R., Volkamer, R., Kille, N., Neu-

man, J. A., Eilerman, S. J., Crawford, J. H., Yacovitch, T. I., Barrick, J. D., and Scarino, A. J.: Validation of IASI Satellite Ammonia Observations at the Pixel Scale Using In Situ Vertical Profiles, J. Geophys. Res.-Atmos., 126, e2020JD033475, https://doi.org/10.1029/2020JD033475, 2021.

Herrera, B., Bezanilla, A., Blumenstock, T., Dammers, E., Hase, F., Clarisse, L., Magaldi, A., Rivera, C., Stremme, W., Strong, K., Viatte, C., Van Damme, M., and Grutter, M.: Measurement report: Evolution and distribution of NH3 over Mexico City from ground-based and satellite infrared spectroscopic measurements, Atmos. Chem. Phys. Discuss. [preprint], https://doi.org/10.5194/acp-2022-217, in review, 2022.

Hersbach, H., Bell, B., Berrisford, P., Hirahara, S., Horányi, A., Muñoz-Sabater, J., Nicolas, J., Peubey, C., Radu, R., Schepers, D., Simmons, A., Soci, C., Abdalla, S., Abellan, X., Balsamo, G., Bechtold, P., Biavati, G., Bidlot, J., Bonavita, M., De Chiara, G., Dahlgren, P., Dee, D., Diamantakis, M., Dragani, R., Flemming, J., Forbes, R., Fuentes, M., Geer, A., Haimberger, L., Healy, S., Hogan, R. J., Hólm, E., Janisková, M., Keeley, S., Laloyaux, P., Lopez, P., Lupu, C., Radnoti, G., de Rosnay, P., Rozum, I., Vamborg, F., Villaume, S., and Thépaut, J.-N.: The ERA5 global reanalysis, Q. J. Roy. Meteor. Soc., 146, 1999–2049, https://doi.org/10.1002/qj.3803, 2020.

Hoesly, R. M., Smith, S. J., Feng, L., Klimont, Z., Janssens-Maenhout, G., Pitkanen, T., Seibert, J. J., Vu, L., Andres, R. J., Bolt, R. M., Bond, T. C., Dawidowski, L., Kholod, N., Kurokawa, J.-I., Li, M., Liu, L., Lu, Z., Moura, M. C. P., O'Rourke, P. R., and Zhang, Q.: Historical (1750–2014) anthropogenic emissions of reactive gases and aerosols from the Community Emissions Data System (CEDS), Geosci. Model Dev., 11, 369–408, https://doi.org/10.5194/gmd-11-369-2018, 2018.

INECC and SEMARNAT: México, Secretaría del Medio Ambiente de la Ciudad de México, Inventario de Emisiones de la Ciudad de México 2016. Dirección General de Gestión de la Calidad del Aire, Dirección de Programas de Calidad del Aire e Inventario de Emisiones, Ciudad de México, Septiembre 2018, http://www.aire.cdmx.gob.mx/descargas/publicaciones/flippingbook/inventario-emisiones-2016/mobile/inventario-emisiones-2016.pdf (last access: 28 May 2021), 2018.

Jeong, C.-H., Traub, A., Huang, A., Hilker, N., Wang, J. M., Herod, D., Dabek-Zlotorzynska, E., Celo, V., and Evans, G. J.: Long-term analysis of PM$_{2.5}$ from 2004 to 2017 in Toronto: Composition, sources, and oxidative potential, Environ. Pollut., 263, 114652, https://doi.org/10.1016/j.envpol.2020.114652, 2020.

Karydis, V. A., Tsimpidi, A. P., Lei, W., Molina, L. T., and Pandis, S. N.: Formation of semivolatile inorganic aerosols in the Mexico City Metropolitan Area during the MILAGRO campaign, Atmos. Chem. Phys., 11, 13305–13323, https://doi.org/10.5194/acp-11-13305-2011, 2011.

Lanzafame, G. M., Srivastava, D., Favez, O., Bandowe, B. A. M., Shahpoury, P., Lammel, G., Bonnaire, N., Alleman, L. Y., Couvidat, F., Bessagnet, B., and Albinet, A.: One-year measurements of secondary organic aerosol (SOA) markers in the Paris region (France): Concentrations, gas/particle partitioning and SOA source apportionment, Sci. Total Environ., 757, 143921, https://doi.org/10.1016/j.scitotenv.2020.143921, 2021.

Larios, A. D., Chebana, F., Godbout, S., Brar, S. K., Valera, F., Palacios, J. H., Avalos Ramirez, A., Saldoval-Salas, F., Larouche,

J. P., Medina-Hernández, D., and Potvin, L.: Analysis of atmospheric ammonia concentration from four sites in Quebec City region over 2010–2013, Atmos. Pollut. Res., 9, 476–482, https://doi.org/10.1016/j.apr.2017.11.001, 2018.

Lee, P. K. H., Brook, J. R., Dabek-Zlotorzynska, E., and Mabury, S. A.: Identification of the Major Sources Contributing to PM$_{2.5}$ Observed in Toronto, Environ. Sci. Technol., 37, 4831–4840, https://doi.org/10.1021/es026473i, 2003.

McDuffie, E. E., Martin, R. V, Spadaro, J. V, Burnett, R., Smith, S. J., O'Rourke, P., Hammer, M. S., van Donkelaar, A., Bindle, L., Shah, V., Jaeglé, L., Luo, G., Yu, F., Adeniran, J. A., Lin, J., and Brauer, M.: Source sector and fuel contributions to ambient PM$_{2.5}$ and attributable mortality across multiple spatial scales, Nat. Commun., 12, 3594, https://doi.org/10.1038/s41467-021-23853-y, 2021.

Ministry of the Environment, Conservation and Parks: Air Quality Ontario, Ministry of the Environment, Conservation and Parks [data set], http://www.airqualityontario.com/, last access: 29 September 2022.

Molina, L. T., Madronich, S., Gaffney, J. S., Apel, E., de Foy, B., Fast, J., Ferrare, R., Herndon, S., Jimenez, J. L., Lamb, B., Osornio-Vargas, A. R., Russell, P., Schauer, J. J., Stevens, P. S., Volkamer, R., and Zavala, M.: An overview of the MILA-GRO 2006 Campaign: Mexico City emissions and their transport and transformation, Atmos. Chem. Phys., 10, 8697–8760, https://doi.org/10.5194/acp-10-8697-2010, 2010.

Murray, C. J. L., Aravkin, A. Y., Zheng, P., et al.: Global burden of 87 risk factors in 204 countries and territories, 1990–2019: a systematic analysis for the Global Burden of Disease Study 2019, Lancet, 396, 1223–1249, https://doi.org/10.1016/S0140-6736(20)30752-2, 2020.

Nair, A. A. and Yu, F.: Quantification of Atmospheric Ammonia Concentrations: A Review of Its Measurement and Modeling, Atmosphere, 11, 1092, https://doi.org/10.3390/atmos11101092, 2020.

NOM-025-SSA1-2021: NORMA Oficial Mexicana NOM-025-SSA1-2021, Salud ambiental, Criterio para evaluar la calidad del aire ambiente, con respecto a las partículas suspendidas PM$_{10}$ y PM$_{2.5}$. Valores normados para la concentración de partículas suspendidas PM10 y PM$_{2.5}$ en el aire ambiente, como medida de protección a la salud de la población, Diario Oficial de la Federacion 27 octubre 2021, https://www.dof.gob.mx/nota_detalle.php?codigo=5633855&fecha=27/10/2021#gsc.tab=0 (last access: August 2022), 2021.

Ojeda-Castillo, V., Alonso-Romero, S., Mena, L. H.-, Álvarez-Chávez, P. E., and del Real-Olvera, J.: Air Pollution in an Urban Area of Mexico: Sources of Emission (Vehicular, Natural, Industrial, and Brick Production), in Air Pollution, edited by: Olvera, J. D. R., IntechOpen, Rijeka, 2019.

Pai, S. J., Heald, C. L., Pierce, J. R., Farina, S. C., Marais, E. A., Jimenez, J. L., Campuzano-Jost, P., Nault, B. A., Middlebrook, A. M., Coe, H., Shilling, J. E., Bahreini, R., Dingle, J. H., and Vu, K.: An evaluation of global organic aerosol schemes using airborne observations, Atmos. Chem. Phys., 20, 2637–2665, https://doi.org/10.5194/acp-20-2637-2020, 2020.

Paulot, F. and Jacob, D. J.: Hidden Cost of U.S. Agricultural Exports: Particulate Matter from Ammonia Emissions, Environ. Sci. Technol., 48, 903–908, https://doi.org/10.1021/es4034793, 2014.

Petit, J.-E., Favez, O., Sciare, J., Crenn, V., Sarda-Estève, R., Bonnaire, N., Močnik, G., Dupont, J.-C., Haeffelin, M., and Leoz-Garziandia, E.: Two years of near real-time chemical composition of submicron aerosols in the region of Paris using an Aerosol Chemical Speciation Monitor (ACSM) and a multi-wavelength Aethalometer, Atmos. Chem. Phys., 15, 2985–3005, https://doi.org/10.5194/acp-15-2985-2015, 2015.

Petit, J.-E., Amodeo, T., Meleux, F., Bessagnet, B., Menut, L., Grenier, D., Pellan, Y., Ockler, A., Rocq, B., Gros, V., Sciare, J., and Favez, O.: Characterising an intense PM pollution episode in March 2015 in France from multi-site approach and near real time data: Climatology, variabilities, geographical origins and model evaluation, Atmos. Environ., 155, 68–84, https://doi.org/10.1016/j.atmosenv.2017.02.012, 2017.

Pope, C. A., Ezzati, M., and Dockery, D. W.: Fine-Particulate Air Pollution and Life Expectancy in the United States, N. Engl. J. Med., 360, 376–386, https://doi.org/10.1056/NEJMsa0805646, 2009.

Potter, P., Ramankutty, N., Bennett, E. M., and Donner, S. D.: Characterizing the Spatial Patterns of Global Fertilizer Application and Manure Production, Earth Interact., 14, 1–22, https://doi.org/10.1175/2009EI288.1, 2010.

Randerson, J. T., Van Der Werf, G. R., Giglio, L., Collatz, G. J., and Kasibhatla, P. S.: Global Fire Emissions Database, Version 4.1 (GFEDv4), ORNL DAAC [data set], https://doi.org/10.3334/ORNLDAAC/1293, 2017.

Retama, A., Ramos-Cerón, M., Rivera-Hernández, O., Allen, G., and Velasco, E.: Aerosol optical properties and brown carbon in Mexico City, Environ. Sci. Atmos., 2, 315–334, https://doi.org/10.1039/D2EA00006G, 2022.

Salcedo, D., Alvarez-Ospina, H., Peralta, O., and Castro, T.: PM$_1$ Chemical Characterization during the ACU15 Campaign, South of Mexico City, Atmosphere, 9, https://doi.org/10.3390/atmos9060232, 2018.

Sciare, J., d'Argouges, O., Zhang, Q. J., Sarda-Estève, R., Gaimoz, C., Gros, V., Beekmann, M., and Sanchez, O.: Comparison between simulated and observed chemical composition of fine aerosols in Paris (France) during springtime: contribution of regional versus continental emissions, Atmos. Chem. Phys., 10, 11987–12004, https://doi.org/10.5194/acp-10-11987-2010, 2010.

Stein, A. F., Draxler, R. R., Rolph, G. D., Stunder, B. J. B., Cohen, M. D., and Ngan, F.: NOAA's HYSPLIT Atmospheric Transport and Dispersion Modeling System, B. Am. Meteorol. Soc., 96, 2059–2077, https://doi.org/10.1175/BAMS-D-14-00110.1, 2015.

Sutton, M. A., Reis, S., Riddick, S. N., Dragosits, U., Nemitz, E., Theobald, M. R., Tang, Y. S., Braban, C. F., Vieno, M., Dore, A. J., Mitchell, R. F., Wanless, S., Daunt, F., Fowler, D., Blackall, T. D., Milford, C., Flechard, C. R., Loubet, B., Massad, R., Cellier, P., Personne, E., Coheur, P. F., Clarisse, L., Van Damme, M., Ngadi, Y., Clerbaux, C., Skjøth, C. A., Geels, C., Hertel, O., Wichink Kruit, R. J., Pinder, R. W., Bash, J. O., Walker, J. T., Simpson, D., Horváth, L., Misselbrook, T. H., Bleeker, A., Dentener, F., and de Vries, W.: Towards a climate-dependent paradigm of ammonia emission and deposition, Philos. T. R. Soc. Lon. B, 368, 20130166, https://doi.org/10.1098/rstb.2013.0166, 2013.

Van Damme, M., Whitburn, S., Clarisse, L., Clerbaux, C., Hurtmans, D., and Coheur, P.-F.: Version 2 of the IASI NH$_3$ neural network retrieval algorithm: near-real-time and reanalysed datasets, Atmos. Meas. Tech., 10, 4905–4914, https://doi.org/10.5194/amt-10-4905-2017, 2017.

Van Damme, M., Clarisse, L., Whitburn, S., Hadji-Lazaro, J., Hurtmans, D., Clerbaux, C., and Coheur, P.-F.: Industrial and agricultural ammonia point sources exposed, Nature, 564, 99–103, https://doi.org/10.1038/s41586-018-0747-1, 2018.

Van Damme, M., Clarisse, L., Franco, B., Sutton, M. A., Erisman, J. W., Wichink Kruit, R., van Zanten, M., Whitburn, S., Hadji-Lazaro, J., Hurtmans, D., Clerbaux, C., and Coheur, P.-F.: Global, regional and national trends of atmospheric ammonia derived from a decadal (2008–2018) satellite record, Environ. Res. Lett., 16, 55017, https://doi.org/10.1088/1748-9326/abd5e0, 2021 (data available at: https://iasi.aeris-data.fr/nh3r-era5/, last access: 29 September 2022).

Vega, E., Eidels, S., Ruiz, H., López-Veneroni, D., Sosa, G., Gonzalez, E., Watson, J. G., Edgerton, S. A., Gasca, J., Mora, V., Reyes, E., Sánchez-Reyna, G., Villaseñor, R., and Chow, J. C.: Particulate Air Pollution in Mexico City: A Detailed View, Aerosol Air Qual. Res., 10, 193–211, https://doi.org/10.4209/aaqr.2009.06.0042, 2010.

Viatte, C., Wang, T., Van Damme, M., Dammers, E., Meleux, F., Clarisse, L., Shephard, M. W., Whitburn, S., Coheur, P. F., Cady-Pereira, K. E., and Clerbaux, C.: Atmospheric ammonia variability and link with particulate matter formation: a case study over the Paris area, Atmos. Chem. Phys., 20, 577–596, https://doi.org/10.5194/acp-20-577-2020, 2020.

Viatte, C., Petit, J.-E., Yamanouchi, S., Van Damme, M., Doucerain, C., Germain-Piaulenne, E., Gros, V., Favez, O., Clarisse, L., Coheur, P.-F., Strong, K., and Clerbaux, C.: Ammonia and PM$_{2.5}$ air pollution in paris during the 2020 covid lockdown, Atmosphere, 12, 160, https://doi.org/10.3390/atmos12020160, 2021.

von Bobrutzki, K., Braban, C. F., Famulari, D., Jones, S. K., Blackall, T., Smith, T. E. L., Blom, M., Coe, H., Gallagher, M., Ghalaieny, M., McGillen, M. R., Percival, C. J., Whitehead, J. D., Ellis, R., Murphy, J., Mohacsi, A., Pogany, A., Junninen, H., Rantanen, S., Sutton, M. A., and Nemitz, E.: Field inter-comparison of eleven atmospheric ammonia measurement techniques, Atmos. Meas. Tech., 3, 91–112, https://doi.org/10.5194/amt-3-91-2010, 2010.

Wang, Q., Jacob, D. J., Spackman, J. R., Perring, A. E., Schwarz, J. P., Moteki, N., Marais, E. A., Ge, C., Wang, J., and Barrett, S. R. H.: Global budget and radiative forcing of black carbon aerosol: Constraints from pole-to-pole (HIPPO) observations across the Pacific, J. Geophys. Res.-Atmos., 119, 195–206, https://doi.org/10.1002/2013JD020824, 2014.

Yamanouchi, S., Viatte, C., Strong, K., Lutsch, E., Jones, D. B. A., Clerbaux, C., Van Damme, M., Clarisse, L., and Coheur, P.-F.: Multiscale observations of NH$_3$ around Toronto, Canada, Atmos. Meas. Tech., 14, 905–921, https://doi.org/10.5194/amt-14-905-2021, 2021.

Yao, X. and Zhang, L.: Causes of Large Increases in Atmospheric Ammonia in the Last Decade across North America, ACS omega, 4, 22133–22142, https://doi.org/10.1021/acsomega.9b03284, 2019.

Zellweger, C., Hüglin, C., Klausen, J., Steinbacher, M., Vollmer, M., and Buchmann, B.: Inter-comparison of four different carbon monoxide measurement techniques and evaluation of the long-term carbon monoxide time series of Jungfraujoch, Atmos. Chem. Phys., 9, 3491–3503, https://doi.org/10.5194/acp-9-3491-2009, 2009.